Materials Horizons

ROYAL SOCIETY OF CHEMISTRY

COMMUNICATION

View Article Online
View Journal

Cite this: DOI: 10.1039/d6mh00331a

Received 23rd February 2026,
Accepted 11th May 2026

DOI: 10.1039/d6mh00331a

rsc.li/materials-horizons

Decoupling shape retention from polymerization kinetics enables ambient-temperature 3D printing of polystyrene

Vanessa Rosciardi, †[a] Federico Serpe, †[bc] Luca Scozzafava, [b] Yurii Promovych, [c] Marco Costantini, [c] Marco Sasso, [d] Carlo Sabbatini, [d] Roberta Angelini *[a] and Andrea Barbetta *[b]

Polystyrene (PS) is a widely used polymer with numerous structural and functional applications, yet its additive manufacturing remains highly constrained. Conventional Fused Deposition Modeling (FDM) relies on the extrusion of pre-polymerized thermoplastic filaments at temperatures exceeding 230 °C, due to the high softening point of PS, and cannot produce crosslinked architectures. This aspect limits design freedom, energy efficiency, and material performance. Here, we introduce a paradigm-shifting approach for ambient-temperature extrusion of PS using an oil-in-water high internal phase emulsion (HIPE) ink composed of styrene and divinylbenzene dispersed in an aqueous phase. UV irradiation during deposition induces instantaneous crosslinking of the continuous phase, forming a thin hydrogel scaffold that confers structural integrity, while subsequent thermal curing converts the oil phase into dense PS. This dual-curing strategy decouples shape retention from polymerization kinetics, allowing for the printing of complex constructs at room temperature. Compression tests reveal exceptional mechanical performance, with a yield stress comparable to that of benchmark FDM polymers (ABS and PETG) and a maximum compressive stress exceeding their values by more than twofold, highlighting the robustness of interlayer cohesion achieved through *in situ* crosslinking. Beyond PS, this versatile approach could unlock new possibilities for scalable, energy-efficient manufacturing of advanced polymer architectures, redefining the boundaries of additive manufacturing.

New concepts

This work introduces a universal, dual-curing, energy-efficient strategy that enables the high-fidelity 3D printing of thermoset polymers, exemplified here by crosslinked polystyrene. The conceptual shift lies in moving from the need to melt pre-polymerized filaments, as required in Fused Deposition Modeling (FDM), to the extrusion of a colloidal monomer-based ink at ambient temperature. Rapid UV-driven stabilization of a thin external shell of the printed filament is followed by a mild thermal curing of the crosslinked core, allowing the construct to retain its shape throughout printing. This approach represents a breakthrough in currently available 3D printing methods, enabling for the first time the direct ink writing of crosslinked polystyrene. A notable outcome of our method is the emergence of superior interlayer adhesion, reflected in mechanical properties exceeding those of benchmark FDM polymers by more than twofold, and in the ability to fabricate challenging overhangs without sacrificial supports. Most importantly, by decoupling printing from polymerization, the method overcomes fundamental kinetic barriers, extending the range of printable materials to virtually any monomer/crosslinker system and enabling continuous multimaterial constructs, even when components exhibit widely different curing kinetics.

Introduction

Additive manufacturing has revolutionized polymer processing, enabling the production of complex geometries and customized designs.[1,2] However, this technology remains fundamentally constrained by the nature of the materials it employs.[3] Conventional extrusion-based methods, such as Fused Deposition Modeling (FDM), rely on thermoplastic filaments that must be melted and deposited layer by layer.[4] For amorphous polystyrene (PS), this requires extrusion temperatures exceeding 230 °C due to its high softening point (≈240 °C) and glass transition near 100 °C.[5] These conditions not only demand energy-intensive processing but also preclude the formation of crosslinked architectures,[6] limiting dimensional stability and chemical resistance.[7] As a result, PS, despite its ubiquity and desirable properties, has been largely excluded from advanced additive manufacturing workflows.[8]

[a] *Institute for Complex Systems – National Research Council (ISC-CNR) and Physics Department, "La Sapienza" University of Rome, Piazzale Aldo Moro 5, 00185 Rome, Italy. E-mail: roberta.angelini@cnr.it*
[b] *Department of Chemistry, "La Sapienza" University of Rome, Piazzale Aldo Moro 5, 00185 Rome, Italy. E-mail: andrea.barbetta@uniroma1.it*
[c] *Institute of Physical Chemistry – Polish Academy of Sciences, Marcina Kasprzaka 44/52, 01224 Warsaw, Poland*
[d] *Department of Industrial Engineering and Mathematical Sciences, Polytechnic University of Marche, via Brecce Bianche 12, 60131 Ancona, Italy*
† Vanessa Rosciardi and Federico Serpe equally contributed to this article.

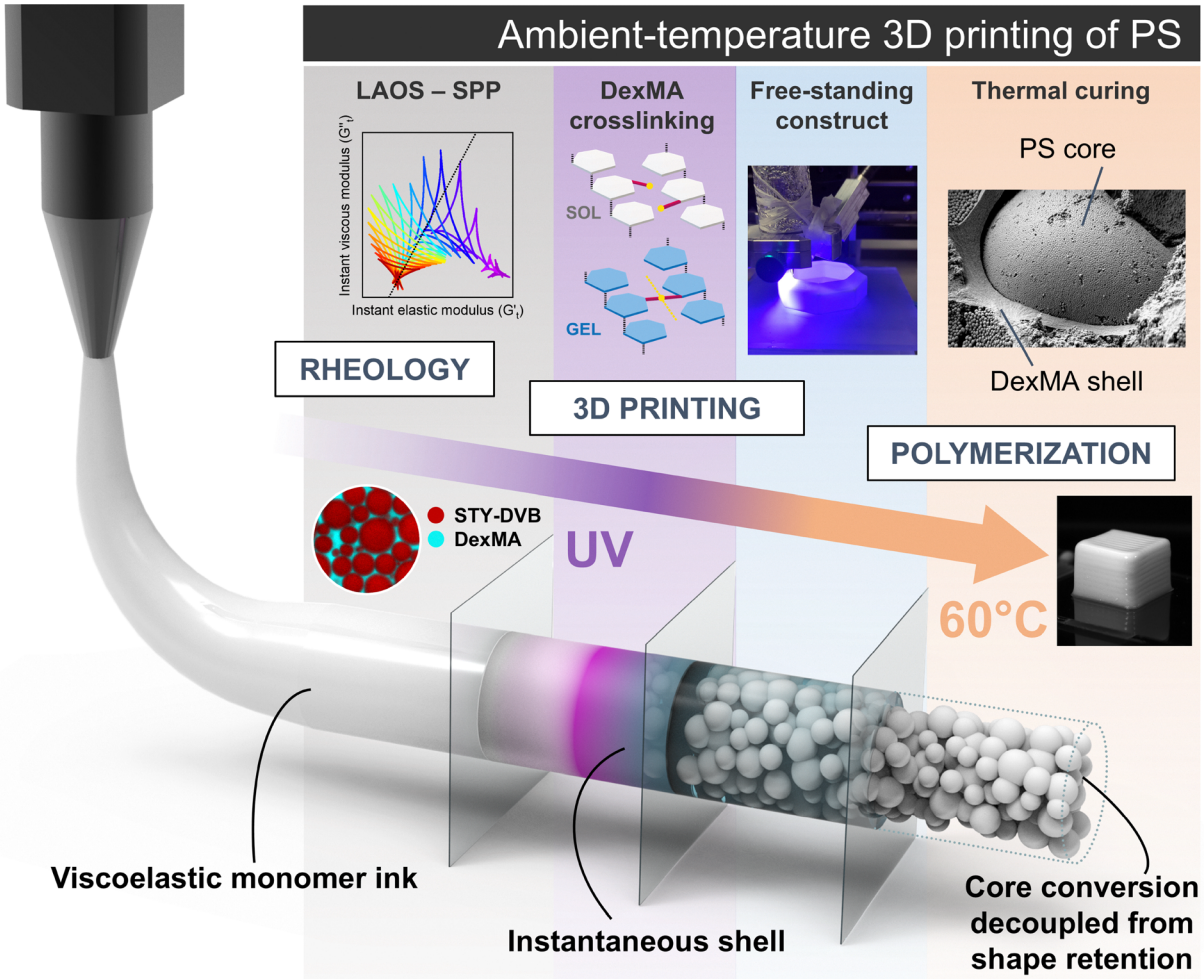

Fig. 1 Overview of the ambient-temperature printing strategy for polystyrene (PS) using HIPE-based inks. The process begins with a viscoelastic high internal phase emulsion (HIPE) ink composed of 85% vol/vol styrene-divinylbenzene (STY-DVB) droplets dispersed in a 15% vol/vol aqueous phase containing methacrylated dextran (DexMA). The oil phase contains a thermal radical initiator, while the water phase contains a photoinitiator. The ink exhibits pronounced non-linear viscoelasticity, as characterized through large amplitude oscillatory shear (LAOS) experiments and interpreted using the Sequence of Physical Processes (SPP) framework, a state-of-the-art method for correlating rheological fingerprints with printing performance. The ink is extruded through the printing nozzle. Upon deposition, UV irradiation triggers instantaneous crosslinking of DexMA, forming a thin hydrogel shell around the emulsion droplets. The rapid stabilization decouples shape retention from the slower polymerization kinetics of styrene, enabling the fabrication of free-standing constructs. Finally, thermal curing at 60 °C converts the internal oil phase into a dense PS core while preserving the external DexMA shell, yielding a hierarchical architecture.

Recent efforts have sought to overcome limitations imposed by FDM by introducing reactive inks and *in situ* polymerization strategies.[9–11] Among these, high internal phase emulsions (HIPEs) have emerged as promising candidates due to their unique rheological behaviour,[12–14] which combines high viscosity with shear-thinning and elasticity, key properties for extrusion printing.[15,16] In our previous work, we demonstrated that HIPEs containing styrene and divinylbenzene (DVB) could serve as stable inks for printing crosslinkable PS-based constructs.[17] This approach represented a paradigm shift, *i.e.*, printing monomers rather than polymers, followed by post-print polymerization. However, the polymerization kinetics of styrene proved incompatible with the fast-printing process, preventing rapid stabilization of the printed filaments. By contrast, in the same study, HIPEs formulated with methacrylate (a blend of methyl methacrylate and hexyl methacrylate) monomers cured almost instantaneously under UV light.

The present work resolves the kinetic bottleneck of styrene through a dual-phase curing strategy (Fig. 1). By incorporating water-soluble methacrylated dextran (DexMA) in the styrene-based HIPE, we introduce a functionality with fast reactivity (methacrylate)[18] in the external phase, enabling UV-induced crosslinking of an ultra-thin hydrogel scaffold around the styrene droplets in the extruded filament. This instantaneous reticulation provides structural integrity at ambient conditions, decoupling shape retention from polymerization kinetics, a fundamental limitation in printing techniques using monomer-containing inks. Subsequent thermal curing at 60 °C completes the polymerization of styrene/DVB within the

oil phase, yielding dense, dimensionally stable PS constructs. This innovation transforms the extrusion printing process from a thermally constrained operation into a modular, room-temperature platform for advanced polymer architectures.

Beyond polystyrene, the implications of this method are profound. Printing monomer-rich inks opens access to a vast library of crosslinked (thermosetting) polymers, which cannot be processed *via* traditional extrusion techniques.[19,20] Moreover, the modularity of HIPE formulations can support multi-material printing using multiple syringes loaded with distinct monomers or monomer mixtures, enabling gradient structures, compositional heterogeneity, and integrated functionalities within a single construct. Ultimately, this approach eliminates the need for energy-intensive melting processes, thereby reducing operational costs and increasing compatibility with low-cost extrusion platforms, which in turn minimizes infrastructure requirements.

Experimental

Chemicals

Dextran (from *Leuconostoc* spp., $M_w \approx 70\,000$ g mol^{-1}), dimethyl sulfoxide (DMSO >99% purity), glycidyl methacrylate (GMA, >97% purity), 4-(*N*,*N*-dimethylamine)pyridine (DMAP, 99%), hydrochloric acid (HCl), styrene (>99% with 4-*tert*-butylcatechol as stabilizer), divinylbenzene (80% purity stabilized with 4-*tert*-butylpyrocatechol), glycerol (>99.5% purity), sodium dodecyl sulfate (SDS, >99% purity), Fluorescein isothiocyanate-dextran (FITC-Dextran, $M_w \approx 70\,000$), Nile Red, 2,2′-azobis(2-methylpropionitrile), (AIBN, 98% purity), Lithium phenyl-2,4,6-trimethylbenzoylphosphinate (LAP, >95% purity), acetone, polystyrene ($M_w \approx 192\,000$ g mol^{-1}) were all purchased from Merck/Sigma-Aldrich. Deionized water was used for sample preparation and dialysis procedures.

Dextran methacrylation

The preparation of methacrylated dextran (DexMA) was conducted following a protocol reported in the literature.[21,22] Briefly, dextran (40 g) was dissolved in DMSO (360 mL) in a sealed round-bottom flask. After dissolution of DMAP (8.0 g), a calculated amount of GMA (10.5 g, equivalent to a theoretical degree of substitution of 30%) was added. The solution was stirred at room temperature for 48 h, after which the reaction was stopped by adding an equimolar amount of concentrated HCl to neutralize the DMAP. The reaction mixture was transferred into a dialysis tube and extensively dialyzed against demineralized water at 4 °C until the nominal conductivity of water was reached. The solution of DexMA was lyophilized, and the obtained product was stored at 4 °C before use. The degree of vinyl functionalization, as determined by ^{1}HNMR, was 25%.

High internal phase emulsions (HIPEs) preparation

Oil-in-water high internal phase emulsions (HIPEs) were prepared by separately formulating the oil and aqueous phases. The oil phase consisted of styrene and divinylbenzene (volume ratio 9 : 1). The aqueous phase consisted of deionized water and glycerol (volume ratio 3 : 2), with sodium dodecyl sulfate (SDS, 5% wt/v relative to the aqueous phase) and DexMA (1, 3, or 5% wt/v) dissolved in the water/glycerol mixture. For samples intended for morphological and rheological characterization, no polymerization initiators were added, and monomers were used as received without removing stabilizers. For samples prepared for 3D printing, lithium phenyl-2,4,6-trimethylbenzoylphosphinate (LAP, 0.5% wt/v relative to the aqueous phase) and azobisisobutyronitrile (AIBN, 0.5% wt/v relative to the oil phase) were incorporated. In this case, styrene and divinylbenzene were purified prior to use by passing them through a basic alumina column under mild vacuum to remove polymerization inhibitors. HIPEs were obtained by dropwise addition of the oil phase into the aqueous phase in a flat-bottomed vessel, maintaining a final phase ratio of 85 vol% oil and 15 vol% aqueous phase. Emulsification was performed under magnetic stirring at 450 rpm, followed by an additional 5 min at 600 rpm to ensure complete homogenization.

Morphological analysis

Morphological characterization of HIPEs was performed using confocal laser scanning microscopy (CLSM). Emulsions were stained with Nile Red (oil phase, 15 μg mL^{-1}) and contained FITC-Dextran in the aqueous phase. Fluorescent images were acquired on an Olympus FV1200 microscope equipped with a solid-state laser (λ = 473 nm and 559 nm) and a photomultiplier tube (PMT) detector (detection range: 485–520 nm for FITC-Dextran and 570–610 nm for Nile Red). A 100× oil-immersion objective (Zeiss) was employed. Samples were mounted in Lab-Tek™ chambered borosilicate cover glass systems (Nalge Nunc International, Rochester, NY, USA) prior to imaging.

Two-dimensional CLSM images were processed using ImageJ software. After binarization with an image-specific threshold, particle analysis was performed *via* the ''Analyze Particles'' plugin. Droplet areas were converted to equivalent diameters to calculate the mean droplet size and size distribution, which was visualized as a 3D histogram. The polydispersity index (PDI) of droplet radii was calculated as:[68]

$$\mathrm{PDI}\ (\%) = \frac{\sqrt{\langle r_{\mathrm{droplet}}{}^2\rangle - \langle r_{\mathrm{droplet}}\rangle^2}}{\langle r_{\mathrm{droplet}}\rangle} \times 100$$

Linear rheological measurements

Rheological characterization was performed using an Anton PaarMCR102rheometer equipped with a cone-plate geometry (cone angle: 2°, diameter: 25 mm). The gap between the cone and plate was set to 0.104 mm, and the temperature was maintained at 22 °C using a Peltier system. An isolation hood and an evaporation blocker were employed to minimize solvent evaporation and sample drying.

Shear-rate-controlled viscosity measurements were conducted over a range of 0.001–1000 s^{-1} following a pre-shear at 500 s^{-1}. Oscillatory tests were performed to determine the storage modulus (G') and loss modulus (G'') within the linear

viscoelastic region (LVE) and to identify deviations from linearity and crossover points. These tests were carried out at angular frequencies of 1, 5, and 15 rad s^{-1} with strain amplitudes varying from 0.1% to 1000%, under constant normal force. All measurements were performed in triplicate, and results are reported as mean values.

Non-linear rheology and sequence of physical processes (SPP) approach

Large Amplitude Oscillatory Shear (LAOS) measurements were performed using the same rheometer setup described above, equipped with the Anton Paar RheoCompass™ software and its LAOS analysis module. Amplitude sweep tests were conducted at a fixed angular frequency of 5 rad s^{-1}, with strain amplitudes ranging from 0.1% to 1000% with a point density of 23. For each imposed strain amplitude, the instrument recorded 513 time-resolved data points corresponding to multiple cycles of sinusoidal strain oscillation from 0 to the maximum strain value (γ_{max}). The raw dataset for each set of 513 points included time, instantaneous strain $\gamma(t)$, stress $\sigma(t)$, and shear rate $\dot{\gamma}(t)$. These data were analysed through an in-house custom python script (reported in SI and deposited on GitHub) using the sequence of physical processes (SPP) framework proposed by Rogers.[43] In SPP, the oscillatory response is treated as a space curve in the three-dimensional deformation space defined by strain, shear rate, and stress $r(t) = (\gamma(t), \dot{\gamma}(t), \sigma(t))$.The local geometry of this curve is described by the Frenet–Serret frame, which consists of the tangent vector $\vec{T}(t)$, the normal vector $\vec{N}(t)$, and the binormal vector $\vec{B}(t)$,

$$\vec{T}(t) = \frac{r'(t)}{\|r'(t)\|} \quad \vec{N}(t) = \frac{\overrightarrow{T'}(t)}{\left\|\overrightarrow{T'}(t)\right\|} \quad \vec{B}(t) = \vec{T}(t) \times \vec{N}(t)$$

The tangent is obtained by normalizing the first derivative of the curve with respect to arc length, the normal by normalizing the derivative of the tangent, and the binormal as the cross product of tangent and normal. These three vectors define the instantaneous orientation of the curve, and the osculating plane spanned by $\vec{T}$ and $\vec{N}$ represents the direction of curvature at each point along the trajectory. Within this osculating plane, the stress evolution is decomposed into components aligned with strain and shear rate, allowing the calculation of instantaneous elastic and viscous moduli. The projection of the curve's motion onto these directions gives

$$\sigma(t) \approx G_t'\gamma(t) + \eta_t\dot{\gamma}(t) \quad G_t'' = \omega\eta_t$$

where G_t' reflects the elastic contribution and G_t'' the viscous contribution, with η_t derived from the shear-rate projection. This geometric approach captures the material's nonlinear behaviour throughout each oscillatory cycle without relying on Fourier decomposition. The resulting pairs of G_t' and G_t'' for each strain cycle are represented in Cole–Cole plots, providing an intuitive visualization of intracycle transitions between solid-like and liquid-like responses.

Printing set-up and printability tests

An in-house 3D printer equipped with an XYZ motor system and a build volume of approximately 10 × 10 × 0.3 cm^3 was controlled *via* Pronterface software. The printer features a custom stainless-steel housing with a central aperture and adjustable screw clamps to securely hold the ink-loaded syringe in alignment with the mechanical deposition system. The feed rate of the printer was set to 900 mm min^{-1}, unless otherwise specified. The syringe (20 mL, KDS stainless steel, Sigma-Aldrich) is fitted with a conical stainless-steel nozzle with a minimum tip diameter of 0.7 mm. The housing also includes four equidistant mounts, one for each UV optical fibre, ensuring uniform illumination at the nozzle tip. Ink extrusion is pneumatically regulated through an OB1 MK4 microfluidic flow controller (Elveflow, France) connected to a nitrogen source. UV source is an OmniCure® S2000 Elite system equipped with a high-pressure 200 W mercury vapor lamp. In the employed configuration, four high-power fibre light guides are coupled to the UV source, each conveying an average irradiance of 18 W cm^{-2} to the nozzle tip (5 mm working distance), as determined from the irradiance spectra provided by the manufacturer. For all printing purposes, the power intensity of the UV reaching the nozzle was set to 5%, corresponding to an irradiance of 0.9 W cm^{-2} for each lightguide. Two-dimensional printability was evaluated through filament fusion tests.[50] In this test, a filament of ink was extruded in a serpentine pattern with progressively increasing spacing between adjacent parallel segments. The aim was to determine the critical distance at which neighbouring filaments cease to fuse and remain distinguishable. Three parameters were considered: the axial distance between adjacent filaments (f_d), the filament thickness (f_t), which served as a normalization factor to account for thickness variations, and the fused segment length (f_s), corresponding to the portion where two adjacent filaments merge. The serpentine geometric code (G-code) was programmed with interfibre distances increasing from 0.2 mm to 3.2 mm in 0.2 mm steps, following the progression $f_{d(n)} = f_{d(n-1)}$ + 0.2 mm. For each sample, three serpentines were printed, photographed orthogonally, binarized, and analysed using ImageJ to calculate f_d, f_t, and f_s. The ratio f_s/f_t was used as a resolution indicator, with values approaching 1 corresponding to the highest resolution and minimal fusion beyond the intended contact points. Results are presented as f_d *versus* f_s/f_t. Ink flow pressure was adjusted to the minimum value, ensuring continuous deposition of an uninterrupted filament, with pressures of 30, 32, 35, and 40 mbar for formulations containing 0, 1, 3, and 5% wt/v DexMA, respectively. These same pressures were applied for 3D printing of cubic samples to assess shape retention and fidelity under conditions with and without UV illumination.

Optimal printing protocol and complex shape printing

After UV-assisted printing of cubic samples, the constructs were subjected to progressively longer post-curing cycles in an Any-Cubic Wash and Cure 3 Plus chamber (36 W). This test allowed

the determination of the optimal curing time for each formulation, as qualitatively assessed by the absence of oil leakage due to overcuring and network shrinkage of DexMA. For the fabrication of complex constructs, the 5% wt/v DexMA formulation was employed, with printing parameters progressively optimized to enable self-standing, non-planar, and overhanging geometries. The final printing protocol consisted of a pressure of 55 mbar, a feed rate of 675 mm min^{-1}, a UV intensity during printing set to 5%, and post-printing UV curing for 1 min. Afterward, constructs were placed in an oven at 60 °C for 6 hours to fully complete the solidification. G-codes for all printed shapes were generated using FullControl G-Code Designer.[69]

Scanning electron microscopy

Polymerized composite constructs based on crosslinked polystyrene were purified *via* Soxhlet extraction with isopropanol for 24 h to remove the surfactant and non-crosslinked monomers, then dried in an oven at 50 °C overnight. The constructs were then mechanically freeze-fractured after immersion in liquid nitrogen to obtain clean internal fracture surfaces. Samples were analysed with a Scanning Electron Microscope (SEM) (Zeiss Auriga, Germany) after cobalt plasma sputtering (Q150T, Quorum Technologie, UK) to create a 25 nm conductive film. Images were acquired using a secondary electron detector at magnifications from 1000× to 40 000×.

Mechanical tests

Mechanical compression tests were performed under quasi-static conditions using an electromechanical universal testing machine (Zwick Z50®), equipped with a 50 kN load cell and compression platens compliant with ASTM D695. All tests were carried out at room temperature under laboratory ambient conditions. The machine crosshead was driven in displacement control at a nominal engineering strain rate of 10^{-3} s^{-1}. The specimens had a nominal parallelepiped geometry, with a square base of 10 mm × 10 mm and a height of 7 mm. Prior to testing, the loading surfaces were carefully machined to ensure flatness and mutual parallelism. A low-friction interface was used between the specimen and the compression plates to limit friction-induced barreling phenomena. In addition to the force–displacement data acquired by the testing machine, deformation measurements were obtained by means of Digital Image Correlation (DIC). During the tests, images of the specimens were acquired at 25 frames per second using a stereo setup consisting of two high-resolution digital cameras (FLIR Blackfly S BFS-U3-88S6M-C®) equipped with Fujinon CF50ZA-1S lenses. The specimen surface preparation, speckle pattern characteristics, illumination conditions, and stereo calibration procedures were defined in accordance with state-of-the-art best practices for DIC.[70] The MatchID® software and toolbox were used for image post-processing and strain evaluation.

Thermal stability and solvent resistance

Thermal stability of 3D-printed cross-linked polystyrene constructs was determined *via* thermogravimetric analysis (TGA 8000, PerkinElmer) and compared to linear bulk polystyrene. The analysis was carried out under an inert atmosphere (constant nitrogen flow, 30.0 mL min^{-1}). The heating ramp was set from 30 to 800 °C with a heating rate of 15 °C min^{-1}. The ramp started after 5 minutes of thermal equilibration of the samples at 30 °C. Solvent resistance was evaluated against acetone for both printed samples and bulk linear PS. For printed samples, the resistance was determined as the weight loss after 24 hours soaking, followed by 6 hours drying at 80 °C. Weight loss was not determined for linear polystyrene as the samples dissolved completely after 24 hours.

Results and discussion

Oil-in-water high internal phase emulsions (HIPEs) were prepared in four formulations, each with a constant oil volume fraction of 0.85 and varying methacrylated dextran (DexMA) content in the aqueous phase (0, 1, 3, and 5% wt/v). The detailed composition is reported in the Experimental Section. HIPEs were obtained by the controlled, dropwise addition of the hydrophobic phase into the aqueous phase under continuous stirring. Methacrylated dextran was synthesized by functionalizing dextran according to a previously reported method,[21,22] yielding a degree of methacrylation of 25%.

Macroscopically, all HIPEs exhibited pronounced viscoelasticity and high yield stress, as evidenced by their resistance to flow when the formulation vial was tilted. Confocal microscopy confirmed the formation of the characteristic jammed structure associated with HIPEs (Fig. S1), where the dispersed oil domains exceed the theoretical packing limit of 0.74.[23,24] For imaging, Dextran functionalized with fluorescein isothiocyanate (FITC-Dextran) was introduced in the aqueous phase while the oil phase was stained with Nile Red. Morphological analysis revealed that both the mean droplet radius and polydispersity index decreased with increasing DexMA content (Fig. S1). This trend is consistent with the relationship:[25]

$$R \propto \frac{\gamma_i}{\eta_{\mathrm{eff}}(\dot{\gamma})\,\dot{\gamma}} (\text{for Ca} \geq \text{Ca}_{\mathrm{crit}})$$

where R is the droplet radius, γ_i the oil–water interfacial tension, and $\eta_{\mathrm{eff}}(\dot{\gamma})$ the shear-dependent viscosity of the continuous phase that accounts for the non-Newtonian nature of the glycerol-, surfactant- and DexMA-containing water phase. When the critical capillary number (Ca_{crit} is exceeded, the initially large oil drops elongate into cylinders and subsequently break into smaller droplets.[26] A higher DexMA content in water translates into an increase in the viscosity of the external phase,[27] which enhances droplet breakup, resulting in finer and more uniform HIPE microstructures.[28]

A preliminary rheological characterization using a cone-plate geometry revealed that all HIPE-based formulations exhibit pronounced elasticity and high viscosity, accompanied by a strong shear thinning behaviour. Amplitude sweep tests showed high storage modulus values (G', around 400 Pa) in the linear viscoelastic region (Fig. S2), indicating a highly structured network capable of resisting deformation under

moderate strains. Rotational flow experiments confirmed that viscosity decreases markedly with increasing shear rate (Fig. S3), a feature essential for extrusion-based 3D printing as it ensures smooth flow through the nozzle while maintaining structural integrity at rest.[29] These properties (high elasticity at low strain and shear-thinning under flow) are fundamental prerequisites for printability.[30] However, conventional rheological metrics provide only a partial view of material behaviour and cannot fully capture the dynamic sequence of stresses and deformations that occur during printing.[31] Extrusion is not a single event but a continuum of processes that can be conceptually mapped onto four stages:[32,33] (i) the ink rests in the syringe in its most structured state; (ii) pressure initiates flow and triggers yielding; (iii) the ink accelerates through a contraction and then a narrow nozzle, undergoing intense shear that fluidizes its microstructure; (iv) finally, once deposited, the ink must rapidly recover elasticity to maintain shape fidelity. These transitions (*i.e.*, from solid-like to fluid-like and back) are central to printability yet are not described by steady-state or small-amplitude oscillatory tests.[31]

Large-amplitude oscillatory shear (LAOS) experiments replicate this sequence of deformation and relaxation,[34] subjecting the material to alternating phases of loading, yielding, viscous flow, and recovery, conditions that closely mirror those encountered during extrusion. Several approaches have been proposed to interpret non-linear viscoelastic responses under LAOS, the most widely used being Fourier transform (FT) rheology[35–37] and the Chebyshev polynomial decomposition of elastic and viscous stresses.[38,39] FT rheology decomposes the stress waveform into a series of harmonics in the frequency domain, providing a ''fingerprint'' of non-linearity,[40] while the Chebyshev approach expresses the stress response as an orthogonal polynomial series enabling the definition of intra-cycle measures such as strain stiffening or shear thinning.[39,41] Although mathematically rigorous, both methods rely on global averages or harmonic coefficients that mix elastic and viscous contributions, which makes their physical interpretation challenging, especially when transient processes such as yielding and recovery dominate the response.[42]

Firstly proposed by Rogers in 2012,[43] the sequence of physical processes (SPP) approach overcomes these limitations by treating the stress response as a trajectory in a three-dimensional deformation space defined by strain, strain rate, and stress. Fig. 2, panel A(iii) shows the deformation trajectory of a 3% DexMA HIPE at two different strain amplitudes as an example.[44] This trajectory is analysed *via* differential geometry within the Frenet–Serret framework.[45,46] At any point along the deformation trajectory, three orthonormal vectors are constructed: $\vec{T}$ (tangent), indicating the instantaneous direction of motion along the curve; $\vec{N}$ (normal), pointing toward the direction of curvature (how the trajectory bends); $\vec{B}$ (binormal), orthogonal to both $\vec{T}$ and $\vec{N}$ and defining the orientation of the osculating plane (which is in turn defined by the first two vectors). From these vectors, the trajectory orientation can be used to compute the transient elastic and viscous moduli ($G_t^{'}$ and $G_t^{''}$), which represent the instantaneous contribution of strain and strain rate to the stress response. The complete derivation of the instantaneous moduli is provided in the Experimental Section and referenced elsewhere.[43] Unlike global measures, these moduli evolve continuously throughout the oscillation, capturing the material's transitions between solid-like and fluid-like states. When plotted as Cole–Cole curves ($G_t^{'}$ *vs.* $G_t^{''}$), the trajectory typically forms a deltoid shape (Fig. 2, panel A(iii)) whose vertices correspond to critical stages of the printing process:[47] maximum elasticity at rest, yielding onset, full fluidization under high strain rate, and finally recovery (this correspondence is schematically illustrated in Fig. 2, panels A and B). This approach provides a physically meaningful, time-resolved description of non-linear viscoelasticity, making it particularly suited for predicting printability.[34]

Indeed, Jeong *et al.*[47] recently suggested that the values of $G_t^{'}$ at the vertex of the $G_t^{'}$ *vs.* $G_t^{''}$ Cole–Cole deltoids can be associated with the behaviour of a structured viscoelastic fluid during the printing process. Specifically, $G_{t\max}^{'}$ (*i.e.*, the maximum value of $G_t^{'}$, indicated with a red triangle in Fig. 2) is relative to the maximum elasticity of the sample at lower strains (representative of the material state in the syringe reservoir and immediately after exiting the extrusion nozzle). Higher values of $G_{t\max}^{'}$, can be related to an improved elastic response of the extruding fluid, implying that the ink retains a robust structure under repeated flow-rest cycles, contributing to both storage stability and rapid post-extrusion recovery. $G_t^{'}$ at $G_{t\max}^{''}$ (indicated as a yellow star in Fig. 2) describes the sharpness of elastic yielding. More negative values indicate a stronger elastic inversion, reflecting a faster and more abrupt transition from a solid-like to a fluid-like state, thereby pointing to a more rapid flow initiation upon entering the contraction channel. Finally, $G_t^{'}$ at $G_{t\min}^{''}$ (indicated as a light-blue circle in Fig. 2) is relative to the residual elasticity of the ink at maximum strain, *i.e.*, when it's completely fluidized. Higher values of $G_t^{'}$ at $G_{t\max}^{''}$ may indicate an excess in elasticity, which can cause inward tension of the filament (a recoil-like behaviour). This residual tension can induce flow retraction of the filament, thereby affecting the resolution of the printed object.

The contribution of DexMA to said rheological parameters is summarized in Fig. 2, panel B. From top to bottom, $G_{t\max}^{'}$, $G_t^{'}$ at $G_{t\max}^{''}$, and $G_t^{'}$ at $G_{t\min}^{''}$ are reported as a function of strain % and for DexMA content varying from 0% to 5%. All the plots are relative to a fixed frequency of 5 rad s^{-1}. As shown in Fig. 2.B, top panel, $G_{t\max}^{''}$ increases significantly in the presence of DexMA. At 100% strain, values rise from ~70 Pa for 0% DexMA to over 150 Pa for 1% DexMA. Further increases in DexMA content continue to elevate $G_{t\max}^{'}$ at comparable strain levels, albeit with a less pronounced slope. An intriguing feature is the emergence of a plateau in the $G_{t\max}^{'}$ *vs.* strain curve for samples containing 3% and 5% wt/v DexMA. This plateau becomes more extended as DexMA concentration increases, suggesting a polymer-induced stabilization effect in the continuous phase.

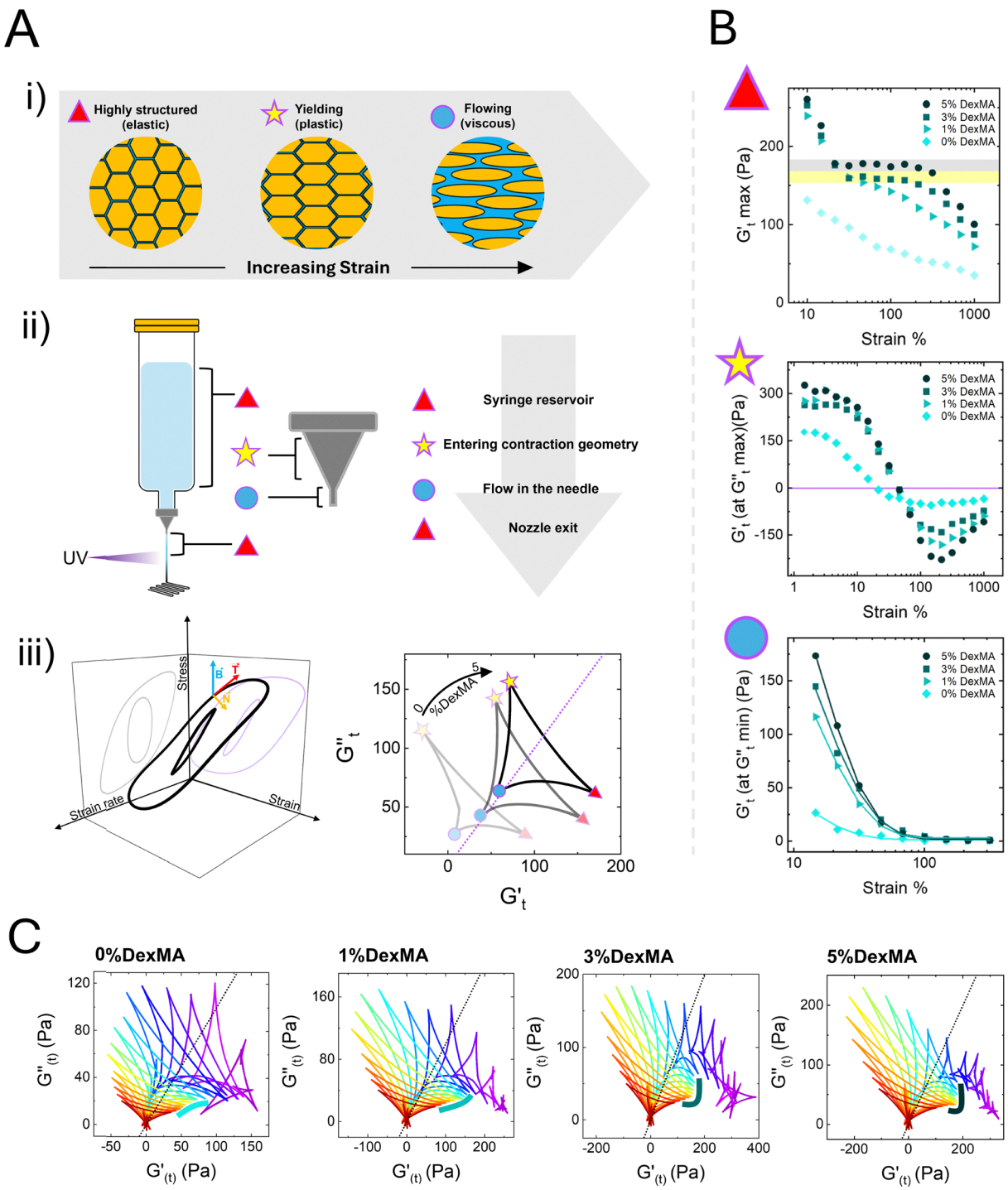

Fig. 2 Nonlinear rheological analysis. (A) (i) Structural transitions of HIPE-based inks under increasing strain, from highly structured (elastic) to yielding and fully fluidized (viscous). Symbols indicate each state and are used throughout the figure to link rheological data to printing stages. At rest, oil domains are tightly packed, and elasticity is at its maximum. As strain increases, domains elongate in the direction of deformation (yielding), and at sufficiently high strain, reciprocal sliding occurs, enabling viscous flow. (A) (ii) Schematic of the extrusion process, mapping structural states to syringe reservoir, contraction zone, nozzle passage, and exit. Each stage corresponds to a specific rheological regime and structural arrangement of the HIPE. (A) (iii) Left: Example of 3D deformation trajectories for 3% wt/v DexMa HIPE at 6.81% and 21.5% strain (5 rad s^{-1}), shown as projections in strain–strain rate–stress space. These trajectories are constructed from strain/stress and strain rate/stress Lissajous plots and can be described by three orthonormal vectors (*T*, *N*, *B*), enabling calculation of instantaneous moduli $\left(G_t^{'}, G_t^{''}\right)$ at any point in the cycle. Right: Cole–Cole plots ($G_t^{'}$ *vs.* $G_t^{''}$) for representative samples (0%, 1%, 3% and 5% DexMa, strain 31.6%, 5 rad s^{-1}). Each deltoid vertex corresponds to a different printing stage and structural state of the HIPE-based ink. (B) Summary of SPP analysis for samples with 0%, 1%, 3%, and 5% wt/v DexMa at 5 rad s^{-1}. From top to bottom: (i) $G_{t\ \max}^{'}$ *vs.* strain (indicator of elastic recovery after extrusion), (ii) $G_t^{'}$ at $G_{t\max}^{''}$ *vs.* strain (sharpness of the transition during flow initiation in the contraction zone), and (iii) $G_t^{'}$ at $G_{t\min}^{''}$ *vs.* strain (residual elasticity at maximum strain, reflecting structural integrity under high deformation). (C) Cole–Cole plots ($G_t^{'}$ *vs.* $G_t^{''}$) for HIPE-based inks containing 0%, 1%, 3%, and 5% wt/v DexMA in the aqueous phase, plotted counterclockwise with increasing strain amplitude (6.81–1000%). Each deltoid represents the intra-cycle evolution of viscoelastic response under LAOS. Highlighted regions on the lower part of the trajectories indicate a "vertical plateau" in $G_{t\max}^{'}$ for formulations with DexMA ≥1%, where elasticity remains nearly constant despite progressively increasing strain, suggesting enhanced structural stabilization under large deformations.

Similar phenomena have been reported for polymer-thickened systems, where macromolecular entanglements enhance elastic recovery under deformation.[48,49] From a practical standpoint, this behaviour indicates that DexMA contributes positively to storage stability and post-extrusion shape retention. As reported in Fig. 2B, middle panel, $G_t^{'}$ at $G_{t\max}^{''}$ exhibits an initial plateau at low strain, followed by an exponential decrease. For the DexMA-free sample, this decline begins around 5% strain, whereas for DexMA-containing formulations (1–5% wt/v), the onset occurs later and follows a similar trend across compositions. Notably, the DexMA-free sample reaches negative $G_t^{'}$ values at lower strain, implying easier flow initiation under moderate shear rates during nozzle contraction. In contrast, DexMA-containing samples display increasingly negative values at high strain, indicating that after an initial resistance, polymer chain alignment facilitates flow—a phenomenon analogous to shear thinning. This suggests that DexMA enhances the formulation's adaptability to extrusion while maintaining structural integrity. The bottom panel shows that $G_t^{'}$ at $G_{t\min}^{''}$ decreases for all samples as strain increases from intermediate ($\sim$12%) to 100%, eventually converging to small positive values. This indicates that none of the formulations exhibit significant recoil tendencies. However, residual elasticity, though minimal, still scales with DexMA content (close-up of the graph in Fig. 4), likely due to viscosity enhancement in the continuous phase. Such viscosity-driven stabilization under stress has been previously observed in HIPE systems.[17] Residual elasticity may thus serve as an indicator of structural integrity preservation, particularly the tight packing of oil domains, which underpins the pronounced elasticity of HIPEs both at rest and under load.

Nonlinear rheological analysis, interpreted through the lens of printability for DexMA-containing formulations, indicates that the most promising system is the one incorporating 5% wt/v DexMA. To validate this prediction, following standard literature protocols, we first performed 2D printability tests to assess the dependence of printing resolution on ink composition, and then conducted qualitative 3D experiments aimed at evaluating overall shape fidelity prior to UV-induced crosslinking of DexMA. An in-house 3D printer was employed for the fabrication process. The printer is equipped with four optical waveguides connected to a UV light source, arranged symmetrically around the nozzle tip to ensure homogeneous UV illumination (Fig. 3, panel A). The ink is loaded into a metallic syringe, and its flow is pneumatically regulated *via* a microfluidic controller connected to a nitrogen source. Technical details of the printing system components are described in the Experimental section.

In the 2D tests (filament fusion test,[50] see Experimental section and SI), image analysis of serpentine filaments deposited at progressively increasing spacing revealed no significant difference in resolution among the inks, suggesting that the addition of DexMA does not measurably affect two-dimensional printing accuracy (Fig. S5). However, the behaviour of inks with varying DexMA content diverged markedly in 3D layer-by-layer deposition trials. Here, the differences in elasticity of DexMA (both at rest and under stress, as previously highlighted by rheology and proportional to DexMA concentration) translated into visibly superior shape retention for the formulation with the highest DexMA content (Fig. 3C, left). This macroscopic observation corroborates rheological predictions, which anticipated enhanced structural integrity of the high internal phase emulsion at elevated DexMA concentrations, particularly in the 5% wt/v DexMA formulation. Maintaining the internal architecture of the concentrated emulsion during printing is crucial for preserving full homogeneity in the final material, thereby preventing phase separation and the uncontrolled formation of segregated polymeric domains that would compromise the mechanical properties of the polymerized construct. Nevertheless, even at 5% wt/v DexMA, shape fidelity is not absolute, but this limitation is effectively mitigated by our printing strategy. During extrusion, the thin layer of continuous phase undergoes rapid UV crosslinking, forming a supporting hydrogel scaffold that fully stabilizes the structure. As shown in Fig. 3 (panel C, middle) UV exposure during extrusion/deposition dramatically enhances printing fidelity across all formulations, with improvements scaling with DexMA content. This trend reflects the role of DexMA in forming the external crosslinked network that provides immediate structural reinforcement. Despite the clear positive contribution of DexMA, it is important to note that in this study only its concentration in the continuous phase varied, while the degree of methacrylation remained constant at approximately 25%. Consequently, aqueous solutions containing different amounts of fully cross-linked DexMA would form hydrogel networks of different densities, resulting in different extents of shrinkage upon curing. Excessive crosslinking could induce significant contraction of the external phase, potentially causing syneresis (expulsion of water)[51,52] or, in extreme cases, acting like an over-compressed sponge that forces the oil phase (styrene and divinylbenzene) out of its compartments and toward the surface of the printed filament.

To prevent such undesired effects, precise control of UV exposure during printing is essential.[53] For all formulations, we standardized the process by employing four UV optical fibres operating at the minimum power allowed by the system (5% of the available intensity, see Experimental section). This level of irradiation proved sufficient to maintain the structural fidelity of simple cubic constructs. To further enhance stabilization before thermal polymerization of the internal phase, printed samples were subjected to additional UV exposure in a curing chamber for progressively increasing intervals of 1, 5, and 10 minutes. As shown in Fig. S6 and schematically summarized in Fig. 3, the 5% wt/v DexMA sample exhibited visible oil leakage after more than one minute of post-print curing, likely due to excessive crosslinking of the external DexMA network. Consistently, the 3% wt/v DexMA formulation showed leakage only after 5 minutes, whereas the 1% wt/v DexMA sample remained stable across all tested intervals. Considering the trade-off between rheological performance, layer-by-layer fidelity, and UV reactivity, we selected the 5% wt/v DexMA formulation for printing complex constructs under a standardized protocol: UV

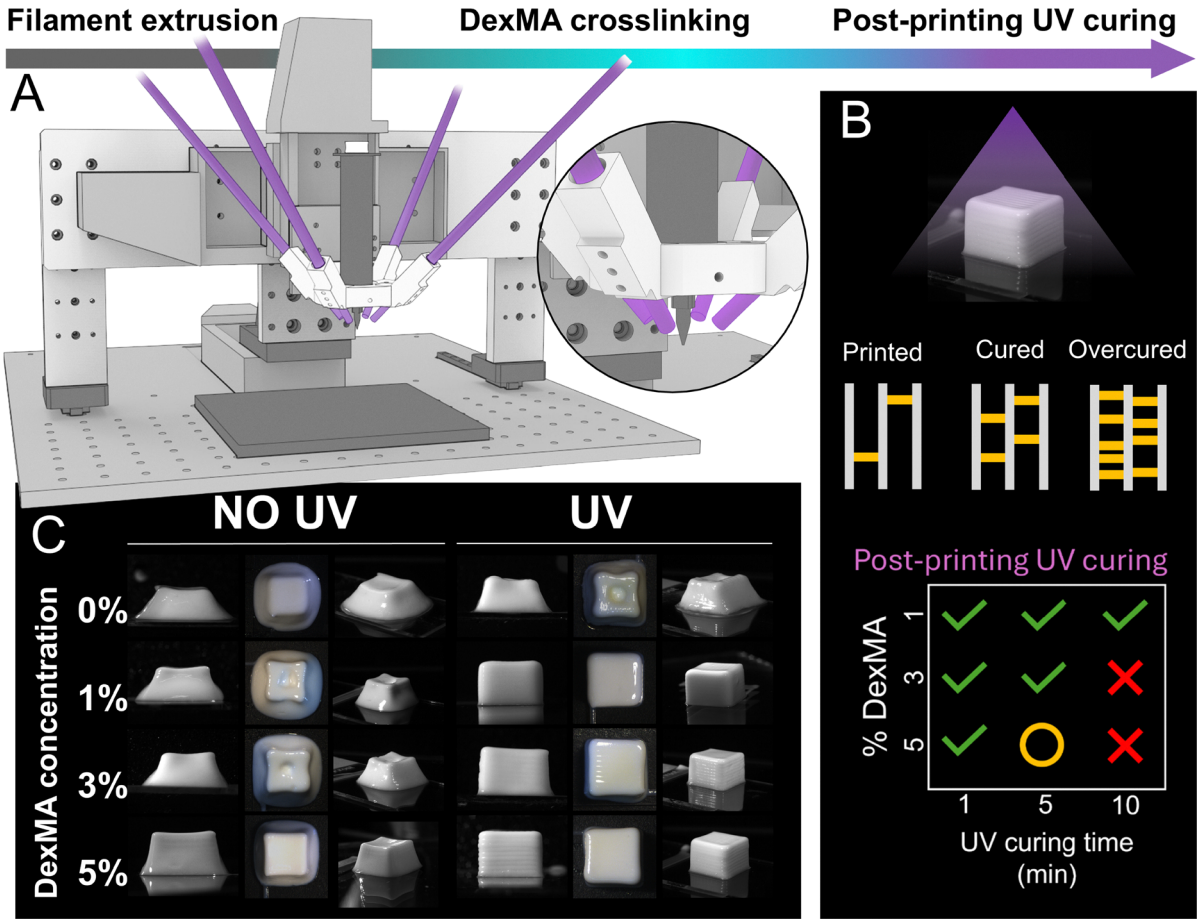

Fig. 3 UV-assisted stabilization of HIPE-based inks during and after extrusion. (A) custom-built extrusion platform equipped with four UV optical fibres positioned around the nozzle to enable *in situ* crosslinking of the DexMA continuous phase during deposition. The inset highlights the nozzle region and UV irradiation geometry. (B) Post-printing UV curing: following the printing stage, during which constructs are exposed to continuous low-intensity UV, they are subjected to additional curing in a UV chamber for 1–10 min. Excessive curing leads to over-crosslinking and oil-phase leakage. The summary chart (bottom) summarizes optimal post-printing UV curing times for each formulation (green thick: no oil leakage; yellow circle: minimal oil leakage; red cross: extended oil leakage). As expected, lower DexMA concentrations tolerate extended curing, while the 5% wt/v DexMA sample requires minimal exposure (1 min) to avoid over-crosslinking and internal phase expulsion. (C) Influence of DexMA concentration and UV exposure on 3D shape fidelity. Constructs printed without UV exhibit a progressive improvement in dimensional stability with increasing DexMA content, consistent with rheological predictions that higher polymer concentration enhances elasticity and recovery. Under UV exposure, all formulations show markedly improved fidelity, with the 5% wt/v DexMA ink producing near-perfect cubic geometries.

exposure at 5% power during extrusion, followed by a 1 minute curing step in the curing chamber. The constructs were then polymerized in an oven at 60 °C for 6 hours to fully convert the oil phase into dense, cross-linked polystyrene.

The 5% wt/v DexMA formulation was initially employed to fabricate simple constructs, *i.e.*, cubic specimens with 1 cm edge length. Printing was performed following the UV-exposure protocol described above, using a pneumatic pressure of 40 mbar, which was empirically determined as the minimum required to deposit a continuous filament during preliminary 2D printability tests. After the complete process, including thermal curing at 60 °C to polymerize styrene-divinylbenzene, the cubic constructs exhibited excellent shape fidelity compared to their counterparts exposed only to UV irradiation, negligible shrinkage (Fig. S7), and demonstrated remarkable reproducibility (see Fig. 4, panel A, for the uniformity of the replicated constructs). Quasi-static compression tests on parallelepiped specimens exhibited a smooth and continuous transition from the elastic regime to strain hardening, without the occurrence of a distinct yield plateau. A representative engineering stress–strain response is reported in Fig. S8. From the initial linear region, the elastic modulus (E) was estimated to be approximately 850 MPa. Upon further deformation, the material sustained compressive stresses exceeding 100 MPa at strains of about 40% (0.4 mm mm^{-1}). The absence of brittle failure and the gradual increase in stress with strain suggest efficient stress redistribution across the sample, pointing towards the existence of a multiscale organization in the tested material.[54] Scanning electron microscopy (SEM) analysis conducted on metallized samples (Fig. 4, panel B) revealed a hierarchical architecture. At the macro/mesoscale the structure consists of distorted spherical poly(styrene-*co*-divinylbenzene)

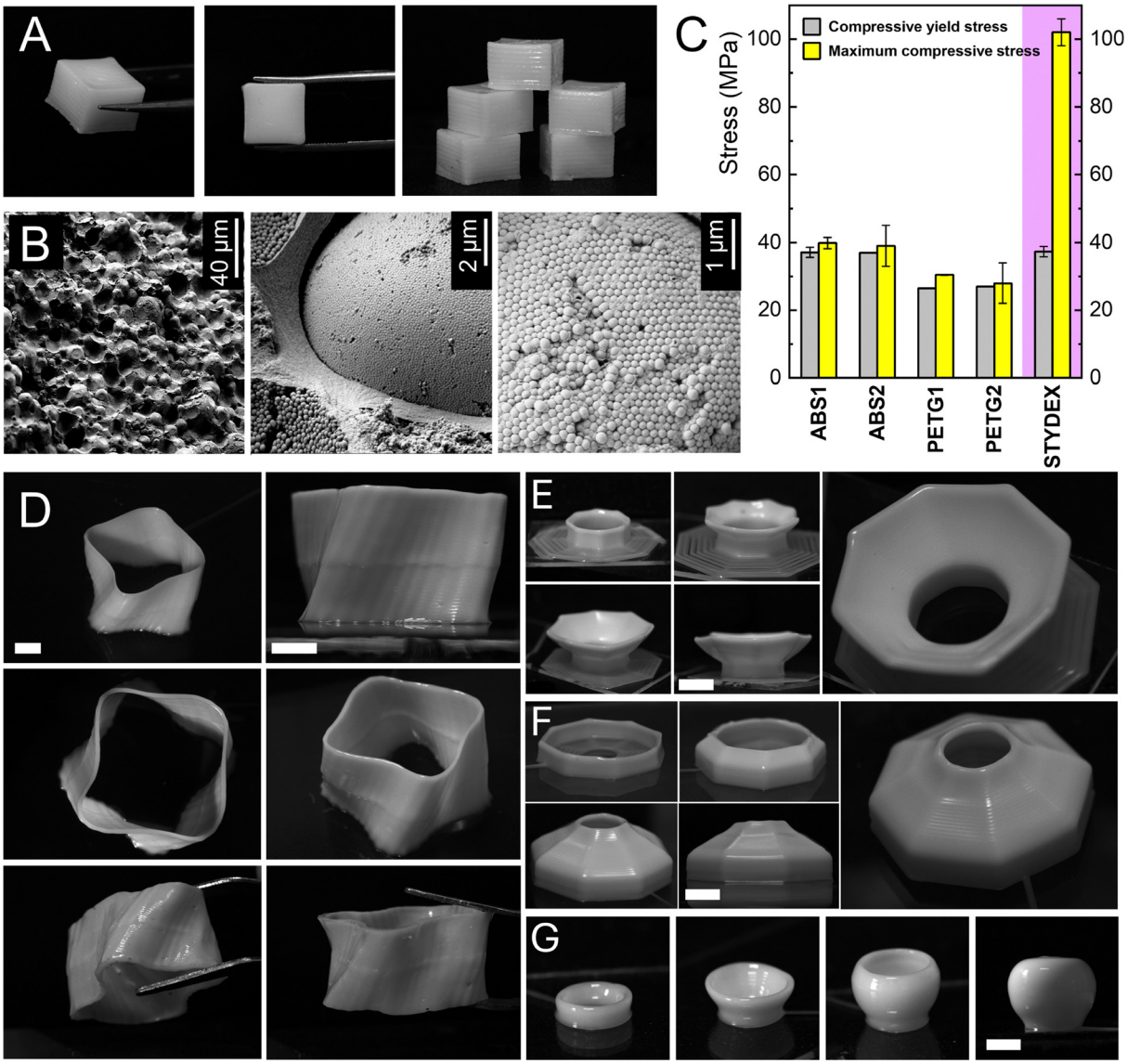

Fig. 4 Printed constructs, hierarchical structure, and mechanical behaviour. (A) Polymerized cubic specimens highlighting the fidelity and reproducibility of the printing, curing, and polymerization process. (B) SEM micrographs of the printed, fully polymerized material at different magnifications, revealing its hierarchical structure: from left to right, macro/mesoscale arrangement of poly(styrene-*co*-divinylbenzene) domains embedded in a thin DexMA, and detail of a single domain composed of densely packed nanospheres (~20 nm), forming highly ordered arrangements approaching hexagonal close packing. (C) Comparison between yield stresses and maximum stresses of FDM printed constructs made of benchmark materials (ABS – Acrylonitrile Butadiene Styrene, and PETG – Polyethylene Terephthalate Glycol) and the same values calculated from the compressive mechanical tests conducted on our polymerized cubic specimens (STYDEX – highlighted in purple in the graph). Values for ABS and PETG are reproduced from recent literature: ABS1 (Kholil *et al.*, 2022),[58] ABS2 (Mishra *et al.*, 2024),[60] PETG1 (Zisopol, 2024),[59] PETG2 (Mishra *et al.*, 2024).[60] In all the cited works, the specimens were produced with the same infill density (100%) and printing layer orientation used for the preparation of our tested samples. (D–G) Examples of challenging free-standing geometries fabricated using the 5% wt/v DexMA formulation, including twisted shapes with rippled walls (D), overhanging structures (outward overhang E, inward overhang F), and a hollow sphere (G). The multiple pictures of E–G refer to the same construct, captured at different printing stages or from different perspectives, to appreciate the inner and outer details and better visualize the objects' dimensions. All the reported scale bars correspond to 1 cm. These constructs demonstrate the ink's ability to maintain dimensional fidelity under gravitational stress without the need for supporting baths; closed cavities, steep overhangs, and multi-angle geometries underscore the synergy between ink viscoelasticity and interlayer crosslinking, enabling unprecedented design freedom for ambient-temperature printing of polystyrene.

domains embedded within a thin dextran-based matrix. The size of these polymerized domains closely matches that of their liquid precursors in the original HIPE (diameters ranging from 4 to 8 μm, as determined by CLSM, Fig. S1). This correspondence arises because the droplet size remains locked within the rapidly gelled aqueous phase during UV exposure upon extrusion, preserving the morphology of the HIPE template. Higher magnification revealed a second level of organization: each micrometric domain is composed of densely packed, highly monodisperse nanospheres (~200 nm in diameter). The

packing density is so high that, at extreme magnification, the nanospheres appear deformed into hexagonal shapes, forming nearly perfect hexagonal close-packed (HCP) arrangements. This configuration, together with face-centred cubic (FCC), represents the most efficient packing mode for monodispersed spheres at the theoretical maximum volume fraction of 0.74.[55] The presence of these nanodomains is attributable to an emulsion polymerization mechanism of styrene, consistent with the well-known Harkins pathway[56,57] and previously observed in styrene-based oil-in-water HIPEs in our earlier work.[17]

A comparative analysis of the compressive properties of our printed samples against benchmark FDM polymers (ABS – Acrylonitrile Butadiene Styrene, and PETG – Polyethylene Terephthalate Glycol) was performed using values reported in the literature for specimens printed with the same infill density (100%) and identical layer deposition pattern,[58–60] ensuring meaningful comparison. As reported in Fig. 4C, our constructs exhibited yield stress values comparable to those of ABS and PETG, confirming the structural potential of the proposed dual-curing approach. More strikingly, the maximum compressive stress, defined as the peak stress on the stress–strain curve, was consistently more than twice that of the reference materials. This enhancement likely stems from superior interlayer cohesion achieved through *in situ* crosslinking of the HIPE ink's continuous phase during deposition. Unlike conventional FDM, where rapid cooling of extruded filaments limits thermal bonding and weakens interlayer adhesion, our strategy promotes robust fusion between adjacent layers. This effectively mitigates a critical failure mode in FDM-printed components (*i.e.*, interlayer delamination), enabling the fabrication of mechanically resilient structures. Moreover, being crosslinked, our constructs are inherently resistant to solvents and exhibit increased thermal stability compared to linear polystyrene (Fig. S9).

After confirming the fidelity of the ink and the reproducibility of the overall process through simple constructs, we proceeded to print four complex geometries, representing well-documented challenges in additive manufacturing:[61–63] (i) a twisted shape with rippled walls (Fig. 4, panel D, left), (ii) an outward free-standing overhang at 45°, (iii) an inward free-standing overhang at 45°, and (iv) a fully closed spherical structure (Fig. 4, panel G, from left to right). These complex constructs were printed with high fidelity to their CAD models, highlighting the ink's ability to withstand gravitational stresses during the fabrication of objects featuring steep overhangs or fully enclosed cavities. Notably, all shapes were produced *via* straightforward extrusion printing (Video S1) without the use of any supporting bath or sacrificial structures, a requirement for most techniques involving polymer printing.[64–67]

It is also important to emphasize that all complex constructs shown in Fig. 4 consist of walls formed by a single ink filament, making their resistance to vertical loads even more remarkable. This extraordinary performance likely stems from the interplay between the composition of the ink's external phase and its overall viscoelasticity. Upon extrusion, the ink is in its most fluid state, and deposition onto the underlying layer can induce slight filament spreading before the elastic recovery predicted by rheological data occurs. This spreading and recovery mechanism coincides temporally with the onset of crosslinking in the external phase, which remains partially uncrosslinked in the underlying filament or, in the case of free-standing overhangs, in adjacent filaments. Given the ink's ability to print suspended in air and nearly horizontally, it is highly plausible that adjacent filaments form interlayer crosslinked junctions, conferring exceptional structural stability and enabling the fabrication of geometries with challenging angles without the need for sacrificial structures (SI, Videos S2–S4).

Conclusions

We have demonstrated a strategy for ambient-temperature printing of polystyrene by decoupling the shape retention of the printed constructs from their polymerization kinetics. Incorporating methacrylated dextran (DexMA) into styrene/divinylbenzene HIPE inks enables rapid UV-induced crosslinking of the continuous phase during deposition, forming a stabilizing thin hydrogel scaffold while the oil phase undergoes subsequent thermal polymerization. This approach enables the printing of complex constructs at room temperature with high shape fidelity, overcoming the limitations of conventional thermoplastic processing. Non-linear rheology, interpreted through the sequence of physical processes (SPP) framework, revealed that DexMA concentration governs intracycle elasticity and recovery, directly correlating with printing performances. The formulation containing 5% wt/v DexMA (with respect to the water phase) provided the best performance, enabling free-standing geometries with challenging overhangs without the need for supporting structures. Importantly, this method enables the extrusion-based fabrication of crosslinked polystyrene, which is currently inaccessible to other techniques. The resulting constructs are inherently resistant to solvents and heating, making them promising for applications requiring chemical and thermal stability, such as filtration membranes, catalyst supports, and components for electrochemical devices. Beyond polystyrene, the same principle can be extended to other monomer–crosslinker systems. Decoupling shape retention from polymerization kinetics enables combining inks with different monomer compositions, even those with widely different curing rates, within a single printing protocol. This opens the door to multi-material constructs and graded architectures with the potential to integrate functionalities that confer additional chemical or mechanical responsiveness. By leveraging HIPE modularity and multi-injection printing systems, this approach enables spatial control of composition and functionality without resorting to energy-intensive processing, thereby expanding the design space for advanced polymer additive manufacturing.

Author contributions

Vanessa Rosciardi: conceptualization, methodology, software, data curation, investigation, formal analysis, writing – original

draft, writing – review and editing. Federico Serpe: investigation, methodology, data curation, writing – original draft, formal analysis, visualization, conceptualization, writing – review and editing. Luca Scozzafava: investigation, methodology. Yurii Promovych: methodology, resources. Marco Costantini: writing – review and editing, validation, resources. Marco Sasso: investigation, validation, funding acquisition. Carlo Sabbatini: investigation, formal analysis. Roberta Angelini: supervision, funding acquisition, writing – review and editing. Andrea Barbetta: conceptualization, funding acquisition, supervision, writing – review and editing, methodology, project administration.

Conflicts of interest

The authors declare no competing financial interests or personal relationships that could have appeared to influence the work reported in this paper.

Data availability

Additional experimental data are provided in the supplementary information (SI). Supplementary information is available. See DOI: https://doi.org/10.1039/d6mh00331a.

The Python code used for the Sequence of Physical Processes (SPP) analysis is deposited on GitHub, available at https://github.com/vanessarosciardi/LAOS_SPP. A Zenodo DOI has been assigned to this repository, and it is available at https://doi.org/10.5281/zenodo.18681438. Raw datasets are available from the authors upon reasonable request.

Acknowledgements

CNIS (Research Center for Nanotechnologies Applied to Engineering, Sapienza University of Rome) is gratefully acknowledged for providing access to scanning electron microscopy (SEM) facilities and technical support. Giancarlo Ruocco, Simone De Panfilis and the Center for Life Nano- & Neuro-Science – CLN2S, IIT (Italian Institute of Technology, Rome) are gratefully acknowledged for providing access to confocal laser scanning microscopy (CLSM) facilities and technical support. A.B., R.A., and M.S. acknowledge financial support under the National Recovery and Resilience Plan (PNRR), Mission 4, Component 2, Investment 1.1, Call for tender No. 104 published on February 2, 2022 by the Italian Ministry of University and Research (MUR), funded by the European Union – NextGenerationEU – Project PRIN 2022ZA77J2 ICARUS – CUP B53D23009010006. A.B. acknowledges financial support from Sapienza University of Rome, Ateneo 2024 funds, N°RM12419112CDC234. F.S. acknowledges financial support from Sapienza University of Rome, *Avvio alla Ricerca*, grant no. AR22419078AC2B88. V.R. acknowledges financial support under the National Recovery and Resilience Plan (PNRR), Mission 4, Component 2, Investment 1.2, Young Researchers – project SOE2024_0000147, BiFuelleD, CUP B83C25001210005. This work was supported by the National Science Centre Poland (NCN) with OPUS 19, grant no. 2020/37/b/st8/02167 to M.C.

References

1 S. S. Banerjee, S. Burbine, N. K. Shivaprakash and J. Mead, *Polymers*, 2019, **11**(2), 347, DOI: 10.3390/polym11020347.
2 S. Park, W. Shou, L. Makatura, W. Matusik and K. Fu, *Matter*, 2022, **5**(1), 43–76, DOI: 10.1016/j.matt.2021.10.018.
3 R. Monzón Mario and Paz, in *Springer Handbook of Additive Manufacturing*, ed. E. Pei, A. Bernard, D. Gu, C. Klahn, M. Monzón, M. Petersen and T. Sun, Springer International Publishing, Cham, 2023, pp. 571–584.
4 P. Siemiński, in *Additive Manufacturing*, ed. J. Pou, A. Riveiro and J. P. Davim, Elsevier, 2021, pp. 217–275.
5 M. Al-Hussein and G. Strobl, *Macromolecules*, 2002, **35**(5), 1672–1676, DOI: 10.1021/ma011345k.
6 A. Sola, *Macromol. Mater. Eng.*, 2022, **307**(10), 2200197, DOI: 10.1002/mame.202200197.
7 Y. Li, Y. Fan and J. Ma, *Polym. Degrad. Stab.*, 2001, **73**(1), 163–167, DOI: 10.1016/S0141-3910(01)00.
8 D. V. A. Ceretti, Y. W. Marien, M. Edeleva, A. La Gala, L. Cardon and D. R. D'hooge, *Sustainability*, 2022, **14**(23), 15488, DOI: 10.3390/su142315488.
9 C. Li, C. Feng, L. Zhang, L. Zhang and L. Wang, *Polym. Eng. Sci.*, 2025, **65**(2), 431–454, DOI: 10.1002/pen.27038.
10 L. Li, Q. Lin, M. Tang, A. J. E. Duncan and C. Ke, *Chem. – Eur. J.*, 2019, **25**(46), 10768–10781, DOI: 10.1002/chem.201900975.
11 C. W. Visser, D. N. Amato, J. Mueller and J. A. Lewis, *Adv. Mater.*, 2019, **31**(46), 1904668, DOI: 10.1002/adma.201904668.
12 X. Li, X. Xu, L. Song, A. Bi, C. Wu, Y. Ma, M. Du and B. Zhu, *ACS Appl. Mater. Interfaces*, 2020, **12**(40), 45493–45503, DOI: 10.1021/acsami.0c11434.
13 G. Cidonio, M. Costantini, F. Pierini, C. Scognamiglio, T. Agarwal and A. Barbetta, *J. Mater. Chem. C*, 2021, **9**(37), 12489–12508, DOI: 10.1039/D1TC02117F.
14 Y. Wang, F. Guo, H. Li, Z. Tang, Y. Cheng and W. Li, *Int. J. Biol. Macromol.*, 2025, **297**, 139975, DOI: 10.1016/j.ijbiomac.2025.139975.
15 C. Duty, C. Ajinjeru, V. Kishore, B. Compton, N. Hmeidat, X. Chen, P. Liu, A. A. Hassen, J. Lindahl and V. Kunc, *J. Manuf. Process.*, 2018, **35**, 526–537, DOI: 10.1016/j.jmapro.2018.08.008.
16 H. Zhang, F. Ye, F. Chen, W. Yuan and W. Yan, *Addit Manuf*, 2024, **81**, 103992, DOI: 10.1016/j.addma.2024.103992.
17 V. Rosciardi, F. Serpe, S. De Panfilis, A. Barbetta and R. Angelini, *J. Colloid Interface Sci.*, 2026, **706**, 139571, DOI: 10.1016/j.jcis.2025.139571.
18 V. Charlot, A. Ibrahim, X. Allonas, C. Croutxé-Barghorn and C. Delaite, *Polym. Chem.*, 2014, **5**(21), 6236–6243, DOI: 10.1039/C4PY00550C.
19 Y. Sun, L. Wang, Y. Ni, H. Zhang, X. Cui, J. Li, Y. Zhu, J. Liu, S. Zhang, Y. Chen and M. Li, *Nat. Commun.*, 2023, **14**(1), 245, DOI: 10.1038/s41467-023-35929-y.
20 Z. Jiang, B. Diggle, M. L. Tan, J. Viktorova, C. W. Bennett and L. A. Connal, *Adv. Sci.*, 2020, **7**(17), 2001379, DOI: 10.1002/advs.202001379.

21 C. Palocci, A. Barbetta, A. La Grotta and M. Dentini, *Langmuir*, 2007, **23**(15), 8243–8251, DOI: 10.1021/la700947g.
22 W. N. E. van Dijk-Wolthuis, O. Franssen, H. Talsma, M. J. van Steenbergen, J. J. Kettenes-van den Bosch and W. E. Hennink, *Macromolecules*, 1995, **28**(18), 6317–6322, DOI: 10.1021/ma00122a044.
23 N. R. Cameron and D. C. Sherrington, *Biopolymers Liquid Crystalline Polymers Phase Emulsion*, Springer Berlin Heidelberg, Berlin, Heidelberg, 1996, pp. 163–214.
24 H. Gao, L. Ma, C. Cheng, J. Liu, R. Liang, L. Zou, W. Liu and D. J. McClements, *Trends Food Sci. Technol.*, 2021, **112**, 36–49, DOI: 10.1016/j.tifs.2021.03.041.
25 C. F. Welch, G. D. Rose, D. Malotky and S. T. Eckersley, *Langmuir*, 2006, **22**(4), 1544–1550, DOI: 10.1021/la052207h.
26 G. I. Taylor, *Proc. R. Soc. Lond. Ser.*, 1934, **146**(858), 501–523, DOI: 10.1098/rspa.1934.0169.
27 V. Tirtaatmadja, D. Dustan and D. Boger, *J. Non-Newton. Fluid*, 2001, **97**(2), 295–301, DOI: 10.1016/S0377-0257(00)00226-3.
28 S. Tripathi, A. Bhattacharya, R. Singh and R. F. Tabor, *Chem. Eng. Sci.*, 2017, **174**, 290.
29 P. A. Amorim, M. A. d'Ávila, R. Anand, P. Moldenaers, P. Van Puyvelde and V. Bloemen, *Bioprinting*, 2021, **22**, e00129, DOI: 10.1016/j.bprint.2021.e00129.
30 P. Wei, C. Cipriani, C.-M. Hsieh, K. Kamani, S. Rogers and E. Pentzer, *J. Appl. Phys.*, 2023, **134**(10), 100701, DOI: 10.1063/5.0155896.
31 M. I. Calafel, M. Criado-Gonzalez, R. Aguirresarobe, M. Fernández and C. Mijangos, *Mater. Adv.*, 2025, **6**(14), 4566–4597, DOI: 10.1039/D5MA00019J.
32 A. Schwab, R. Levato, M. D'Este, S. Piluso, D. Eglin and J. Malda, *Chem. Rev.*, 2020, **120**(19), 11028–11055, DOI: 10.1021/acs.chemrev.0c00084.
33 M. E. Cooke and D. H. Rosenzweig, *APL Bioeng.*, 2021, **5**(1), 011502, DOI: 10.1063/5.0031475.
34 Y. Liu, M. Hildner, O. Roy, W. A. Van den Bogert, J. Lorenz, M. Desroches, K. Koppi, A. Shih and R. G. Larson, *J. Rheol.*, 2023, **67**(4), 791, DOI: 10.1122/8.0000612.
35 T. Liang, A. I. Isayev and J. Zhong, *Polymer*, 2023, **267**, 125670, DOI: 10.1016/j.polymer.2022.125670.
36 E. García-Tuñón, R. Agrawal, B. Ling and D. J. C. Dennis, *Phys. Fluids*, 2023, **35**(1), 017113, DOI: 10.1063/5.0128658.
37 D. M. Hoyle, D. Auhl, O. G. Harlen, V. C. Barroso, M. Wilhelm and T. C. B. McLeish, *J. Rheol.*, 2014, **58**(4), 969–997, DOI: 10.1122/1.4881467.
38 A. M. Le, M. Y. Erturk and J. Kokini, *J. Food Eng.*, 2023, **336**, 111193, DOI: 10.1016/j.jfoodeng.2022.111193.
39 A. Eid, M. M. Khader and A. M. Megahed, *Open Phys.*, 2024, **22**(1), 20240001, DOI: 10.1515/phys-2024-0001.
40 D. J. da Silva, G. S. Michelini, R. C. L. de Sá and A. H. Ferreira, *Carbohydr. Polym.*, 2026, **373**, 124598, DOI: 10.1016/j.carbpol.2025.124598.
41 S. O. Ilyin, *Polym. Sci. Ser. A*, 2015, **57**(6), 910–923.
42 Q. Zhang, L. Jiang and X. Sui, *Food Hydrocolloids*, 2023, **135**, 108177, DOI: 10.1016/j.foodhyd.2022.108177.
43 S. A. Rogers, *J. Rheol.*, 2012, **56**(5), 1129–1151, DOI: 10.1122/1.4726083.
44 J. Choi, F. Nettesheim and S. A. Rogers, *Phys. Fluids*, 2019, **31**(7), 073107, DOI: 10.1063/1.5106378.
45 J. D. Park and S. A. Rogers, *Phys. Fluids*, 2020, **32**(6), 063102, DOI: 10.1063/5.0006792.
46 G. Arreaga, R. Capovilla and J. Guven, *Class Quantum Gravity*, 2001, **18**(23), 5065, DOI: 10.1088/0264-9381/18/23/304.
47 E. H. Jeong, J. Choi, H. B. Park, J. W. Lee, S. Y. Bae, B. S. Kim, C. Yoon and J. D. Park, *Adv. Sci.*, 2025, e07639, DOI: 10.1002/advs.202507639.
48 S. O. Ilyin, *Polymers*, 2024, **16**(17), 2458, DOI: 10.3390/polym16172458.
49 J. C.-W. Lee, L. Porcar and S. A. Rogers, *AIChE J.*, 2019, **65**(12), e16797, DOI: 10.1002/aic.16797.
50 A. Ribeiro, M. M. Blokzijl, R. Levato, C. W. Visser, M. Castilho, W. E. Hennink, T. Vermonden and J. Malda, *Biofabrication*, 2018, **10**(1), 014102, DOI: 10.1088/1758-5090/aa90e2.
51 K. Ako, S. Elmarhoum and C. D. Munialo, *Food Hydrocolloids*, 2022, **124**, 107346, DOI: 10.1016/j.foodhyd.2021.107346.
52 Z. Qin, Y. Yang, Z. Zhang, F. Li, Z. Hou, Z. Li, J. Shi and T. Shen, *Gels*, 2025, **11**(10), 780, DOI: 10.3390/gels11100780.
53 A. Barkane, O. Platnieks, M. Jurinovs, S. Kasetaite, J. Ostrauskaite, S. Gaidukovs and Y. Habibi, *Polymers*, 2021, **13**(8), 1195, DOI: 10.3390/polym13081195.
54 W. Lu, Q. Zhang, F. Qin, P. Xu, Q. Chen, H. Wang, F. Scarpa and H.-X. Peng, *Appl. Mater. Today*, 2021, **25**, 101222, DOI: 10.1016/j.apmt.2021.101222.
55 I. Sanchez-Burgos, E. Sanz, C. Vega and J. R. Espinosa, *Phys. Chem. Chem. Phys.*, 2021, **23**(35), 19611–19626, DOI: 10.1039/D1CP01784E.
56 W. D. Harkins, *J. Chem. Phys.*, 1945, **13**(9), 381–382, DOI: 10.1063/1.1724054.
57 L. Peng, M. Wu, J. Lu, A. Zhang, K. Zhang and S. Ma, *Langmuir*, 2025, **41**(4), 2651–2660, DOI: 10.1021/acs.langmuir.4c04437.
58 A. Kholil, E. Asyaefudin, N. Pinto and S. Syaripuddin, *J. Phys. Conf. Ser.*, 2022, **2377**, 012001, DOI: 10.1088/1742-6596/2377/1/012001.
59 D. G. Zisopol, M. Minescu and D. V. Iacob, *Eng., Technol. Appl. Sci. Res.*, 2024, **14**(2), 13592–13597, DOI: 10.48084/etasr.7063.
60 V. Mishra, N. Bharat, V. Kumar, D. Veeman and M. Vellaisamy, *Phys. Scr.*, 2024, **99**(12), 125033, DOI: 10.1088/1402-4896/ad8fe0.
61 J. Jiang, J. Stringer, X. Xu and R. Y. Zhong, *Int. J. Comput. Integr. Manuf.*, 2018, **31**(10), 961–969, DOI: 10.1080/0951192X.2018.1466398.
62 J. Ye, X. Lin, H. Lu, H. Shen, Z. Wang and Y. Zhao, *Structures*, 2024, **59**, 105699, DOI: 10.1016/j.istruc.2023.105699.
63 H. Quan, T. Zhang, H. Xu, S. Luo, J. Nie and X. Zhu, *Bioact. Mater.*, 2020, 5(1), 110–115, DOI: 10.1016/j.bioactmat.2019.12.003.
64 W. Hua, K. Mitchell, L. Raymond, B. Godina, D. Zhao, W. Zhou and Y. Jin, *ACS Biomater. Sci. Eng.*, 2021, **7**(10), 4736–4756, DOI: 10.1021/acsbiomaterials.1c00910.
65 J. Zhao and N. He, *J. Mater. Chem. B*, 2020, **8**(46), 10474–10486.
66 G. Nayyar, C. B. Williams and T. E. Long, *Polymer*, 2025, **326**, 128355, DOI: 10.1016/j.polymer.2025.128355.

67 K. Fu, *Acc. Mater. Res.*, 2025, **6**(8), 921–926, DOI: 10.1021/accountsmr.5c00156.
68 S. Andrieux, W. Drenckhan and C. Stubenrauch, *Langmuir*, 2018, **34**(4), 1581–1590, DOI: 10.1021/acs.langmuir.7b03602.
69 A. Gleadall, *Addit. Manuf.*, 2021, **46**, 102109, DOI: 10.1016/j.addma.2021.102109.
70 M. Sutton and F. Hild, *Exp. Mech.*, 2015, **55**(1), 1–8, DOI: 10.1007/s11340-015-9991-6.